

PS-NeRF: Neural Inverse Rendering for Multi-view Photometric Stereo

Wenqi Yang¹ Guanying Chen^{2*} Chaofeng Chen³
Zhenfang Chen⁴ Kwan-Yee K. Wong¹

¹The University of Hong Kong ²FNii and SSE, CUHK-Shenzhen
³Nanyang Technological University ⁴MIT-IBM Watson AI Lab

Abstract. Traditional multi-view photometric stereo (MVPS) methods are often composed of multiple disjoint stages, resulting in noticeable accumulated errors. In this paper, we present a neural inverse rendering method for MVPS based on implicit representation. Given multi-view images of a non-Lambertian object illuminated by multiple unknown directional lights, our method jointly estimates the geometry, materials, and lights. Our method first employs multi-light images to estimate per-view surface normal maps, which are used to regularize the normals derived from the neural radiance field. It then jointly optimizes the surface normals, spatially-varying BRDFs, and lights based on a shadow-aware differentiable rendering layer. After optimization, the reconstructed object can be used for novel-view rendering, relighting, and material editing. Experiments on both synthetic and real datasets demonstrate that our method achieves far more accurate shape reconstruction than existing MVPS and neural rendering methods. Our code and model can be found at <https://ywq.github.io/psnerf>.

Keywords: Multi-view photometric stereo, inverse rendering, neural rendering

1 Introduction

Multi-view stereo (MVS) is a technique for automated 3D scene reconstruction from a set of images captured from different viewpoints. As MVS methods rely on feature matching across different images, they generally assume the scene to be composed of textured Lambertian surfaces [45,12,1] and their reconstructions often lack fine details. Photometric stereo (PS), on the other hand, can recover per-pixel surface normals of a scene from single-view images captured under varying light directions. By utilizing shading information, PS method can recover fine surface details for both non-Lambertian and textureless objects [56,14,46]. However, single-view PS methods are not capable of recovering a full 3D shape.

To combine the merits of both techniques, multi-view photometric stereo (MVPS) methods are proposed to recover high-quality full 3D shapes for non-Lambertian and textureless objects [11,41,26]. Traditional MVPS methods are

* Corresponding author

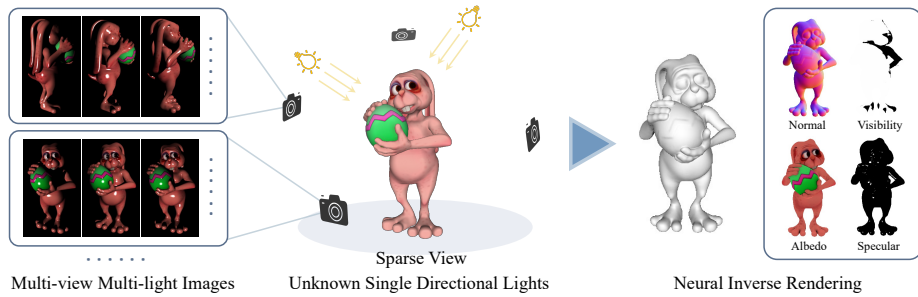


Fig. 1. Our method takes multi-view multi-light images as input, and is able to reconstruct accurate surface and faithful BRDFs based on our shadow-aware renderer. Specifically, we only take images under **sparse** views with each view illuminated by multiple **unknown** single directional lights.

often composed of multiple disjoint stages [26,41], leading to noticeable accumulated errors.

Neural rendering methods have recently been introduced to tackle the problems of multi-view reconstruction and novel-view synthesis [60,39,36]. These methods work on multi-view images captured under fixed illuminations and show spectacular results. In addition to viewing directions, Kaya *et al.* [23] use surface normals estimated from an observation map-based PS method to condition the neural radiance field (NeRF). Although improved rendering results have been reported, this method has 4 fundamental limitations, namely 1. it requires calibrated lights as input to estimate per-view normal maps; 2. it takes surface normals as inputs for NeRF, making novel-view rendering difficult (if not impossible); 3. it does not recover BRDFs for the surface, making it not suitable for relighting; and 4. the PS network and NeRF are disjointed, and normal estimation errors from PS network will propagate to NeRF and cannot be eliminated.

To solve these challenges, we propose a neural inverse rendering method for multi-view photometric stereo (See Fig. 1). Our method does not require calibrated lights. We first estimate per-view normal maps to constrain the gradient of density in NeRF. Surface normals, BRDFs, and lights are then jointly optimized based on a shadow-aware differentiable rendering layer. By taking advantage of both multi-view and multi-light images, our method achieves far more accurate shape reconstruction results. Moreover, as our method explicitly models BRDFs and lights, it allows novel-view rendering, relighting, and material editing.

In summary, the key contributions of this paper are as follows:

- We introduce a neural inverse rendering method for multi-view photometric stereo, which jointly optimizes shape, BRDFs, and lights based on a shadow-aware differentiable rendering layer.
- We propose to regularize the surface normals derived from the radiance field with normals estimated from multi-light images, which significantly improves surface reconstruction, especially for sparse input views (e.g., 5 views).

- Our method achieves state-of-the-art results in MVPS, and demonstrates that incorporating multi-light information appropriately can produce a far more accurate shape reconstruction.

2 Related Work

Single-view Photometric stereo (PS) Traditional PS methods rely on outlier rejection [58,37,59], reflectance model fitting [51,10,18], or exemplars [15,16] to deal with non-Lambertian surfaces. Deep learning based PS methods solve this problem by learning the surface reflectance prior from a dataset [44,8,17,49,7,31]. These methods typically train a deep network to learn the mapping from image measurements to surface normals. Recently, many efforts have been devoted to reduce the number of images required [25,65] and to estimate light directions in an uncalibrated setup [6,22,33].

Multi-view Photometric Stereo (MVPS) MVPS combines the advantages of MVS and PS methods, leading to more accurate surface reconstructions. Traditional MVPS methods assume a simplified surface reflectance [29,11,57,41,32]. They first apply MVS to reconstruct a coarse shape from multi-view images and adopt PS to obtain per-view surface normals from multi-light images. They then refine the coarse shape using the obtained normals. Zhou *et al.* [26,66] propose a method to deal with isotropic materials. Their method first reconstructs sparse 3D points from multi-view images and identifies per-view iso-depth contours using multi-light images. It then recovers a complete 3D shape by propagating the sparse 3D points along the iso-depth contours. Kaya *et al.* [21] propose an uncertainty-aware deep learning based method to integrate MVS depth maps with PS normal maps to produce a full shape. Another branch of methods adopts a co-located camera-light setup for joint reflectance and shape recovery [9,27,38,53].

Neural Rendering Neural rendering methods have achieved great successes in novel-view synthesis and multi-view reconstruction [50,47,60,39]. In particular, neural radiance field (NeRF) [36] achieves photo-realistic view synthesis by representing a continuous space with an MLP which maps 5D coordinates (*i.e.*, 3D point and view direction) to density and color. Many follow-up works are proposed to improve the reconstructed shape [40,52], rendering speed [30,42,13], and robustness [34,62,2]. However, these methods essentially treat surface points as light sources, and thus cannot disentangle materials and lights [55].

Some methods have been proposed to jointly recover shape, materials, and lights [61,4]. PhySG [61] and NeRD [4] adopt Spherical Gaussian (SG) representation for BRDFs and environment illumination to enable fast rendering. Neural-PIL [5] replaces the costly illumination integral operation with a simple network query. These methods [61,4,5], however, ignore cast shadows during optimization. NeRV [48] explicitly models shadow and indirect illumination, but it requires a known environment map. NeRFactor [64] proposes a learned auto-encoder to represent BRDFs and pre-extracts a light visibility buffer using the

Table 1. Comparisons among different neural inverse rendering methods (MVI stands for multi-view images).

Method	Input	Shape	BRDF	Lighting	Shadow
NeRV [48]	MVI (Fixed lighting)	Density	Microfacet model	Known Envmap	Yes
PhySG [61]	MVI (Fixed lighting)	SDF	Microfacet (SGs)	Unknown Envmap (SGs)	No
NeRFactor [64]	MVI (Fixed lighting)	Density	Learned BRDF	Unknown Envmap	Yes
NeRD [5]	MVI (Varying lighting)	Density	Microfacet (SGs)	Unknown Envmap (SGs)	No
NRF [3]	MVI (Co-located light)	Density	Microfacet model	Known Co-located light	Yes
KB22 [23]	MVI (Multi-light)	Density	No	No	No
Ours	MVI (Multi-light)	Density	Mixture of SGs	Unknown Multi-light	Yes

obtained mesh. NRF [3] optimizes a neural reflectance field assuming a co-located camera-light setup.

Similar to our proposed method, Kaya *et al.* [23] introduce a NeRF-based method for MVPS. Their method [23] assumes calibrated light directions and takes the estimated normals as input to condition their NeRF. It thus cannot disentangle surface materials and light directions. Table 1 summarizes the differences between our method and existing neural inverse rendering methods. Our method is the only one that explicitly models surface reflectances and lights under a multi-view photometric stereo setup.

3 Methodology

3.1 Overview

Given multi-view and multi-light images¹ of an object taken from M sparse views, our goal is to simultaneously reconstruct its shape, materials, and lights. We denote the MVPS image set as \mathcal{I} , and multi-light images for each view m as $\mathcal{I}^m = \{I_1^m, I_2^m, \dots, I_{L_m}^m\}$. Note that the number of lights for each view can vary. Figure 2 illustrates the overall pipeline of our method.

Inspired by the recent success of neural radiance field [36] for 3D scene representation, we propose to represent the object shape with a density field. Our method consists of two stages to make full use of multi-view multi-light images.

In the first stage, we estimate a guidance normal map \mathcal{N}_m for each view, which is used to supervise the normals derived from the density field. This direct normal supervision is expected to provide a strong regularization on the density field, leading to an accurate surface. In the second stage, based on the learned density field as the shape prior, we jointly optimize the surface normals, materials, and lights using a shadow-aware rendering layer.

3.2 Stage I: Initial Shape Modeling

In the first stage, we optimize a neural radiance field with surface normal regularizations to represent the object shape.

¹ *i.e.*, multiple images are captured for each view, where each image is illuminated by a single unknown directional light.

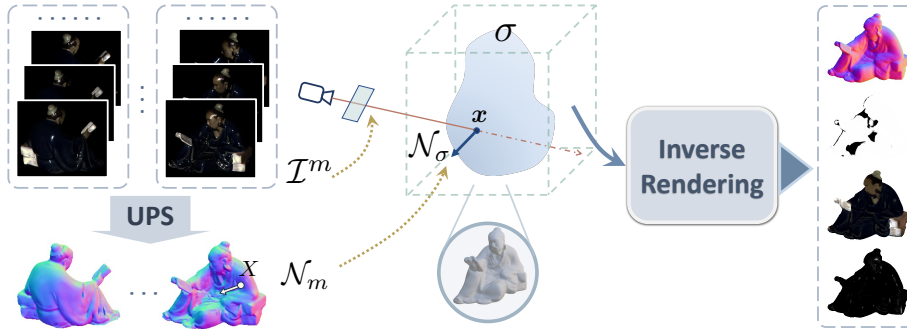


Fig. 2. Given multi-view multi-light images, we first obtain guidance normal maps via uncalibrated photometric stereo (UPS) to regularize the neural density field, which encourages accurate surface reconstruction. We then perform neural inverse rendering to jointly optimize surface normals, BRDFs and lights based on the initial shape.

Neural Radiance Field NeRF employs an MLP to map a 3D point \mathbf{x}_k in space and view direction \mathbf{d} to density σ_k and color \mathbf{c}_k , *i.e.*,

$$(\sigma_k, \mathbf{c}_k) = \text{MLP}_{\text{NeRF}}(\mathbf{x}_k, \mathbf{d}). \quad (1)$$

Given a pixel in an image, its color can be computed by integrating the color of the points sampled along its visual ray \mathbf{r} through volume rendering, *i.e.*,

$$\tilde{\mathbf{C}}(\mathbf{r}) = \sum_{k=1}^K T_k (1 - \exp(-\sigma_k \delta_k)) \mathbf{c}_k, \quad T_k = \exp\left(-\sum_{j=1}^{k-1} \sigma_j \delta_j\right), \quad (2)$$

where $\delta_k = t_{k+1} - t_k$ is the distance between adjacent sampled points.

Typically, a NeRF is fitted to a scene by minimizing the reconstruction error between the rendered image \mathbf{C} and the input image I , *i.e.*,

$$\mathcal{L}'_c = \sum \|\mathbf{C} - I\|_2^2. \quad (3)$$

However, as the surface geometry has no direct supervision, the density field is generally very noisy. Recently, UNISURF [40] improves the surface quality of NeRF by gradually shrinking the sampling range of a ray for volume rendering, leading to a smoother surface. However, as shown in our experiments, the shape recovered by UNISURF [40] is still not satisfactory.

Surface Normal Regularization The above observation motivates us to introduce regularizations for the surface geometry. Notably, state-of-the-art uncalibrated photometric stereo (UPS) method, such as [6], can estimate a good normal map from single-view multi-light images. We therefore use the normal map \mathcal{N}_m estimated by [6] to regularize the density field by minimizing

$$\mathcal{L}'_n = \sum \|\mathcal{N}_\sigma - \mathcal{T}_{m2w}(\mathcal{N}_m)\|_2^2, \quad \mathcal{N}_\sigma(\mathbf{x}) = \frac{\nabla \sigma(\mathbf{x})}{\|\nabla \sigma(\mathbf{x})\|_2}, \quad (4)$$

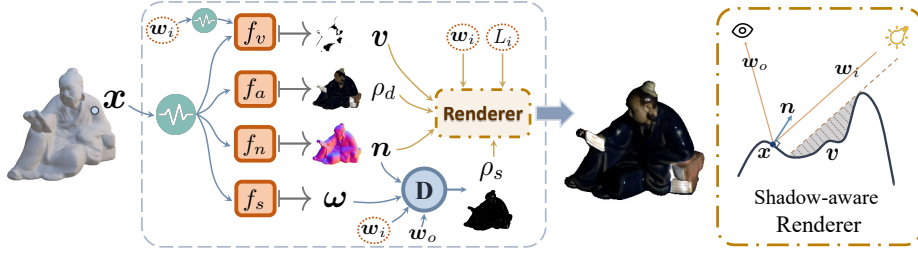


Fig. 3. In Stage II, we model normals, BRDFs, and light visibility of the scene with MLPs. The weights of the MLPs and lights are jointly optimized to fit the input images.

where \mathcal{N}_σ is the surface normal derived from the gradient of the density field σ based on the expected depth location, and \mathcal{T}_{m2w} is transformation that transforms the view-centric normals from the camera coordinate system to the world coordinate system. We also include the normal smoothness regularization [40] with $\epsilon \sim \mathcal{N}(0, 0.01)$, *i.e.*,

$$\mathcal{L}'_{ns} = \sum \|\mathcal{N}_\sigma(\mathbf{x}) - \mathcal{N}_\sigma(\mathbf{x} + \epsilon)\|_2^2. \quad (5)$$

We adopt UNISURF [40] as our radiance field method for initial shape modeling, and the overall loss function for Stage I is given by

$$\mathcal{L}' = \alpha_1 \mathcal{L}'_c + \alpha_2 \mathcal{L}'_n + \alpha_3 \mathcal{L}'_{ns}, \quad (6)$$

where α_* denotes the loss weights.

3.3 Stage II: Joint Optimization with Inverse Rendering

With the initial shape (*i.e.*, σ and \mathcal{N}_σ) from Stage I, we are able to jointly optimize the surface normals, spatially-varying BRDFs, and lights based on a shadow-aware rendering layer (see Fig. 3). Specifically, we first extract the surface from the density field via root-finding [39,35] similar to [40]. We then model surface normals, BRDFs, and light visibility of the scene with MLPs. The weights of the MLPs and the lights are then jointly optimized to fit the input multi-view and multi-light images. In the following subsections, we will describe the formulation of our rendering layer and each component in detail.

Rendering Equation The rendering equation for a non-Lambertian surface point \mathbf{x} can be written as [20]

$$\hat{I}(\mathbf{w}_o; \mathbf{x}) = \int_{\Omega} L_i(\mathbf{w}_i) f_r(\mathbf{w}_o, \mathbf{w}_i; \mathbf{x}) (\mathbf{w}_i \cdot \mathbf{n}) d\mathbf{w}_i, \quad (7)$$

where \mathbf{w}_i and \mathbf{w}_o are the incident light direction and view direction respectively, $f_r(\mathbf{w}_o, \mathbf{w}_i; \mathbf{x})$ represents a general BRDF at location \mathbf{x} . $L_i(\mathbf{w}_i)$ is the light intensity along \mathbf{w}_i and $\hat{I}(\mathbf{w}_o; \mathbf{x})$ is the integrated radiance over the upper-hemisphere Ω .

By assuming a directional light and considering light visibility, the rendering equation can be rewritten as

$$\hat{I}(\mathbf{w}_o, \mathbf{w}_i; \mathbf{x}) = f_v(\mathbf{w}_i; \mathbf{x})L_i(\mathbf{w}_i)f_r(\mathbf{w}_o, \mathbf{w}_i; \mathbf{x})(\mathbf{w}_i \cdot \mathbf{n}), \quad (8)$$

where $f_v(\mathbf{w}_i; \mathbf{x})$ indicates the visibility of light along \mathbf{w}_i at \mathbf{x} , and models cast-shadow in the rendered image.

Shape Modeling In Stage I, we optimize a radiance field with surface normal regularizations to produce an initial density field σ . Note the normals used to regularize \mathcal{N}_σ are estimated by a PS method [6] which inevitably contain estimation errors. As a result, the derived normals \mathcal{N}_σ might not be accurate in some regions. To refine the normals, we use an MLP $f_n(\mathbf{x}) \mapsto \mathbf{n}$ to model the distribution of surface normals. This MLP will be optimized by an image fitting loss. To encourage the refined normals to not deviate too much from the derived normals, we use the derived normals to regularize the output of $f_n(\mathbf{x})$ by minimizing

$$\mathcal{L}_n'' = \sum \|f_n(\mathbf{x}) - \mathcal{N}_\sigma(\mathbf{x})\|_2^2. \quad (9)$$

Visibility Modeling Given the density field σ , a surface point \mathbf{x} , and a light direction \mathbf{w}_i , the light visibility $\mathcal{V}_\sigma(\mathbf{x}, \mathbf{w}_i)$ can be computed by applying volume rendering to calculate the accumulated density along the ray directed from \mathbf{x} to the light source [64].

Since we perform ray-marching to calculate visibility for each point and each query light direction, it will be time-consuming to compute light visibility for an environment map lighting. Besides, the computed visibility might also be noisy. We therefore model the distribution of light visibility using another MLP $f_v(\mathbf{x}, \mathbf{w}_i) \mapsto v$, which is regularized by the computed visibility by minimizing

$$\mathcal{L}_v'' = \|f_v(\mathbf{x}, \mathbf{w}_i) - \mathcal{V}_\sigma(\mathbf{x}, \mathbf{w}_i)\|_2^2. \quad (10)$$

Material Modeling As in previous works [61,4,64], we assume the BRDF model can be decomposed into diffuse color ρ_d and specular reflectance ρ_s , *i.e.*, $f_r(\mathbf{x}, \mathbf{w}_i, \mathbf{w}_o) = \rho_d + \rho_s(\mathbf{x}, \mathbf{w}_i, \mathbf{w}_o)$. For diffuse color, we use an MLP $f_a(\mathbf{x}) \mapsto \rho_d$ to model the albedo for a surface point \mathbf{x} .

For specular component, one may adopt a reflectance model (*e.g.*, Microfacet) to model the specular reflectance and estimate its parameters (*e.g.*, roughness) [48,28]. However, we found it difficult to model the specular effects of real-world objects by directly estimating the roughness parameter. Instead, we propose to fit the specular reflectance with a weighted combination of specular basis following [16,24].

We assume isotropic materials and simplify the input to a half-vector \mathbf{h} and normal \mathbf{n} according to [43], and define a set of Sphere Gaussian (SG) basis as

$$D(\mathbf{h}, \mathbf{n}) = G(\mathbf{h}, \mathbf{n}; \lambda) = \left[e^{\lambda_1(\mathbf{h}^T \mathbf{n} - 1)}, \dots, e^{\lambda_k(\mathbf{h}^T \mathbf{n} - 1)} \right]^T, \quad (11)$$

where $\lambda_* \in \mathcal{R}_+$ denotes specular sharpness. We introduce an MLP $f_s(\mathbf{x}) \mapsto \boldsymbol{\omega}$ to model the spatially-varying SG weights, and specular reflectance can then be recovered as

$$\rho_s = \boldsymbol{\omega}^T D(\mathbf{h}, \mathbf{n}). \quad (12)$$

To encourage a smooth albedo and specular reflectance distribution, we impose smoothness losses \mathcal{L}_{as}^R and \mathcal{L}_{ss}^R (defined similarly as in Eq. (5)) for $f_a(\mathbf{x})$ and $f_s(\mathbf{x})$ respectively.

Light Modeling Each image is illuminated by a directional light, which is parameterized by a 3-vector light direction and a scalar light intensity. We set the light directions and intensities as learnable parameters, and initialize them by the lights estimated by the UPS method [6]. The light parameters will be refined after the joint optimization.

Joint Optimization Based on our scene representation, we can re-render the input images using the differentiable rendering equation. Given multi-view and multi-light images, we optimize the normal, visibility, and BRDF MLPs together with the light parameters to minimize the image reconstruction loss, given by

$$\mathcal{L}_c'' = \sum \|\hat{I} - I\|_2^2, \quad (13)$$

where \hat{I} is the re-rendered image and I is the corresponding input image.

The overall loss function used for our neural inverse rendering stage is

$$\mathcal{L}'' = \beta_1 \mathcal{L}_c'' + \beta_2 \mathcal{L}_n'' + \beta_3 \mathcal{L}_v'' + \beta_4 \mathcal{L}_{as}'' + \beta_5 \mathcal{L}_{ss}'', \quad (14)$$

where β_* denotes the corresponding loss weight.

4 Experiments

4.1 Implementation details

Please refer to supplementary materials for implementation details. We first use all 96 lights for training and evaluation, and then demonstrate that our framework can support arbitrary sparse light sources in Sec. 4.5.

Evaluation Metrics We adopt commonly used quantitative metrics for different outputs. Specifically, we use mean angular error (MAE) in degree for surface normal evaluation under test views, and Chamfer distance for mesh evaluation². Following [40], we extract meshes using the MISE algorithm [35]. PSNR, SSIM [54], and LPIPS [63] are used to evaluate the reconstructed images.

² We rescale the meshes into the range of $[-1, 1]$ for all the objects, and show Chamfer distance in the unit of *mm*).

Table 2. Results of different MVPS methods on DiLiGenT-MV benchmark.

Method	Chamfer Dist.↓					Average	Normal MAE↓					Average
	BEAR	BUDDHA	COW	POT2	READING		BEAR	BUDDHA	COW	POT2	READING	
PJ16 [41]	19.58	11.77	9.25	24.82	22.62	17.61	12.78	14.68	13.21	15.53	12.92	13.83
LZ20 [26]	8.91	13.29	14.01	7.40	24.78	13.68	4.39	11.45	4.14	6.70	8.73	7.08
Ours	8.65	8.61	10.21	6.11	12.35	9.19	3.54	10.87	4.42	5.93	8.42	6.64

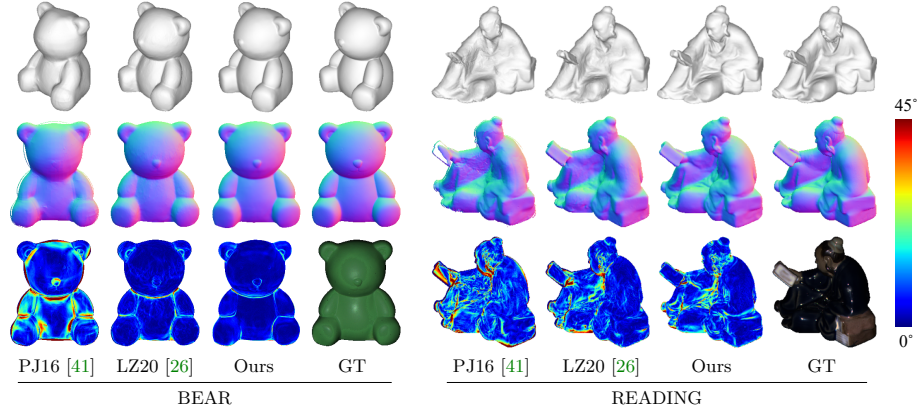


Fig. 4. Qualitative results of shape and normal on DiLiGenT-MV benchmark.

4.2 Dataset

Real Data We adopted the widely used DiLiGenT-MV benchmark [26] for evaluation. It consists of 5 objects with diverse shapes and materials. Each object contains images captured from 20 views. For each view, 96 images are captured under varying light directions and intensities. Ground-truth meshes are provided. In our experiments, we sample 5 testing views with equal interval, and take the rest 15 views for training. Note that our method assumes unknown light direction and light intensity in evaluation.

Synthetic Data To enable more comprehensive analysis, we rendered a synthetic dataset with 2 objects (*i.e.*, *BUNNY*, *ARMADILLO*) with Mitsuba [19]. We rendered objects under two sets of lightings, one with directional lights, denoted as Synth^{PS} dataset, and the other with environment map, denoted as Synth^{Env} dataset. We randomly sampled 20 camera views on the upper hemisphere, where 15 views for training and 5 views for testing. We used directional lights in the same distribution as DiLiGenT-MV benchmark for each view. For the synthetic dataset, we set the same light intensity for each light source.

4.3 Comparison with MVPS Methods

We compared our method with state-of-the-art MVPS methods [26,41] on DiLiGenT-MV benchmark, where all 20 views are used for optimization. It should be noted that our method does not use calibrated lights as [26,41].

Table 2 summarizes the quantitative comparison. The results of Chamfer distance are calculated with ground truth shape. The normal MAE results of

Table 3. Comparison of novel view rendering on the DiLiGenT-MV benchmark.

Method	BEAR			BUDDHA			COW			POT2			READING		
	PSNR \uparrow	SSIM \uparrow	LPIPS \downarrow	PSNR \uparrow	SSIM \uparrow	LPIPS \downarrow	PSNR \uparrow	SSIM \uparrow	LPIPS \downarrow	PSNR \uparrow	SSIM \uparrow	LPIPS \downarrow	PSNR \uparrow	SSIM \uparrow	LPIPS \downarrow
NeRF [36]	30.98	0.9887	1.09	29.31	0.9664	2.80	33.03	0.9907	0.54	32.52	0.9842	1.41	26.58	0.9664	1.84
KB22 [23]	39.63	0.9960	0.24	33.62	0.9844	0.56	31.38	0.9800	0.87	33.39	0.9767	1.02	22.45	0.9560	2.11
UNISURF [40]	40.13	0.9954	0.40	30.98	0.9707	1.98	40.17	0.9953	0.39	43.06	0.9954	0.50	22.19	0.9579	2.29
NeRFactor [61]	29.28	0.9791	2.38	26.34	0.9385	6.33	27.60	0.9630	1.67	32.32	0.9738	1.84	25.62	0.9468	2.99
NeRD [5]	26.24	0.9661	3.56	20.94	0.8701	6.25	23.98	0.8914	1.97	26.34	0.8422	2.19	20.13	0.9023	3.90
PhySG [61]	34.01	0.9841	1.60	29.64	0.9594	2.65	34.38	0.9856	1.02	35.92	0.9814	1.23	24.19	0.9531	2.88
Ours	41.58	0.9959	0.31	33.73	0.9829	0.54	42.39	0.9962	0.22	45.44	0.9960	0.15	30.47	0.9808	0.75

Table 4. Shape reconstruction results of neural rendering methods on both real and synthetic datasets. We use both Synth^{Env} dataset and Synth^{PS} dataset for evaluation.

Method	DiLiGenT-MV										Synthetic							
	BEAR		BUDDHA		COW		POT2		READING		BUNNY		ARMADILLO		PS		Env	
	MAE \downarrow	CD \downarrow	MAE \downarrow	CD \downarrow	MAE \downarrow	CD \downarrow	MAE \downarrow	CD \downarrow	MAE \downarrow	CD \downarrow	MAE \downarrow	CD \downarrow	MAE \downarrow	CD \downarrow	PS	Env	PS	Env
NeRF [36]	73.90	66.68	59.89	29.28	55.14	70.07	69.71	42.28	55.75	48.26	49.42	48.22	19.67	20.09	44.27	41.54	20.95	24.34
KB22 [23]	53.19	66.18	39.72	17.92	85.11	82.43	87.30	63.82	70.13	86.79	31.64	37.00	9.61	18.32	35.88	51.08	14.50	7.58
UNISURF [40]	6.48	9.24	17.11	9.83	8.25	13.25	13.05	10.21	19.72	62.89	10.00	11.46	6.89	8.74	8.12	10.12	3.76	3.96
NeRFactor [61]	12.68	26.21	25.71	26.97	17.87	50.65	15.46	29.00	21.24	47.36	21.97	21.50	17.29	18.29	36.07	19.27	7.86	18.44
NeRD [5]	19.49	13.90	30.41	18.54	33.18	38.62	28.16	9.00	30.83	30.05	17.51	19.12	11.08	13.44	19.36	18.43	7.02	9.34
PhySG [61]	11.22	19.07	26.31	21.66	11.53	22.23	13.74	32.29	25.74	46.90	23.53	25.66	22.23	21.87	14.46	19.53	8.27	12.08
Ours	3.21	7.24	10.10	8.93	4.08	11.33	5.67	5.76	8.83	12.83	5.14	-	5.32	-	5.18	-	3.61	-

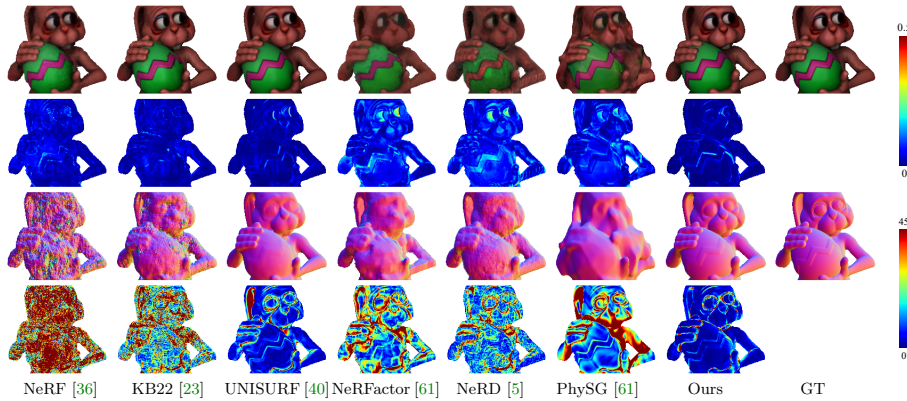


Fig. 5. Novel view rendering and normal estimation results on the synthetic dataset.

DiLiGenT test views are calculated inside the intersection of input mask and our predicted mask. We can see that our method outperforms previous methods in 4 out of 5 objects by a large margin in terms of both two metrics. In particular, our method significantly reduces the Chamfer distance of the most challenging *READING* object from 22.62mm to 12.35mm. On average, our method improves Chamfer distance by 33%, and normal MAE by 6%. Such remarkable performance proves that our method is much better in shape reconstruction than existing approaches. We notice our results of the *COW* object are slightly worse. Detailed discussions are in the supplementary material.

To show the advantages of our method intuitively, we present two visual example comparisons in Figure 4. We show the easiest *BEAR* with a smooth surface and the most challenging *READING* with many wrinkles. It can be observed that our results have fewer noises than LZ20 and PJ16 on the smooth

Table 5. Analysis on normal supervision.

Method	Normal MAE↓						Chamfer Dist↓					
	BEAR	BUDDHA	COW	POT2	READING	BUNNY	BEAR	BUDDHA	COW	POT2	READING	BUNNY
NeRF	73.45	59.62	55.10	69.41	55.55	49.24	66.68	29.28	70.07	42.28	48.26	19.67
NeRF ^{+N}	7.03	13.50	8.26	7.93	14.01	12.04	16.02	9.65	12.04	7.25	13.31	5.44
UNISURF	6.51	17.13	8.26	13.04	19.68	10.04	9.24	9.83	13.25	10.21	62.89	6.89
UNISURF ^{+N}	4.26	11.29	5.05	6.37	9.58	7.76	7.24	8.93	11.33	5.76	12.83	5.32



Fig. 6. Qualitative results of estimated surface normal on w/ or w/o normal supervision.

surface of *BEAR*, and our reconstruction of the detailed wrinkles of *READING* is much better. It demonstrates that our method is superior in reconstructing both smooth and rugged surfaces.

4.4 Comparison with Neural Rendering Based Methods

We also compared our method with existing neural rendering methods, including NeRF [36], KB22 [23], UNISURF [40], PhySG [61], NeRFactor [61], and NeRD [5]. Among them, the first three methods can only support novel-view rendering and cannot perform scene decomposition.

For KB22 [23], we re-implemented it by adding the normals estimated by PS method as input to NeRF following their paper. For other methods, we used their released codes for experiments.

Evaluation on DiLiGenT-MV Benchmark Following the training of our radiance field stage, we use the multi-light averaged image for each view (equivalent to image lit by frontal hemisphere lights) for training and testing the baselines. For our method, we rendered directional light images and computed the light-averaged image for each view in testing phases. As the light intensity can only be estimated up to an unknown scale, we reported the scale-invariant PSNR, SSIM and LPIPS for all methods by first finding a scalar to rescale the rendered image using least-square.

Table 3 and Table 4 show that our method achieves the best rendering and normal estimation results, and significantly outperforms the existing best method UNISURF [40] for shape reconstruction. We attribute the success in view rendering to the faithful decomposition of shape, material, and light components and our shadow-aware design. The multi-light images provide abundant high-frequency information related to the shape and material, which ensures high rendered quality under diverse illuminations.

Table 6. Normal improvement.

Method	BEAR	BUDDHA	COW	POT2	READING	BUNNY
SDPS-Net	7.52	11.47	9.57	7.98	15.94	10.65
Stage I	4.26	11.29	5.05	6.39	9.58	7.79
Ours	3.25	10.20	4.12	5.73	8.87	5.24

Table 7. Light improvement.

Method	BEAR	BUDDHA	COW	POT2	READING	BUNNY
SDPS-Net	4.90	7.17	8.55	4.73	9.09	8.96
Ours	2.27	2.75	2.59	2.89	4.26	1.53

Table 8. Ablation study on Stage II.

Method	BEAR			BUDDHA			COW			POT2			READING			BUNNY		
	PSNR \uparrow	SSIM \uparrow	MAE \downarrow	PSNR \uparrow	SSIM \uparrow	MAE \downarrow	PSNR \uparrow	SSIM \uparrow	MAE \downarrow	PSNR \uparrow	SSIM \uparrow	MAE \downarrow	PSNR \uparrow	SSIM \uparrow	MAE \downarrow	PSNR \uparrow	SSIM \uparrow	MAE \downarrow
fixed-light	34.51	0.9812	3.62	29.48	0.9661	10.51	35.58	0.9872	4.45	39.47	0.9845	5.84	24.58	0.9708	9.18	24.04	0.9833	6.94
w/o vis	33.44	0.9794	3.57	28.06	0.9571	10.29	36.94	0.9890	4.09	39.38	0.9837	5.75	24.49	0.9699	8.91	21.29	0.9761	5.34
Ours	35.68	0.9837	3.25	29.58	0.9670	10.20	37.06	0.9890	4.12	40.01	0.9860	5.73	24.89	0.9725	8.87	25.88	0.9871	5.24

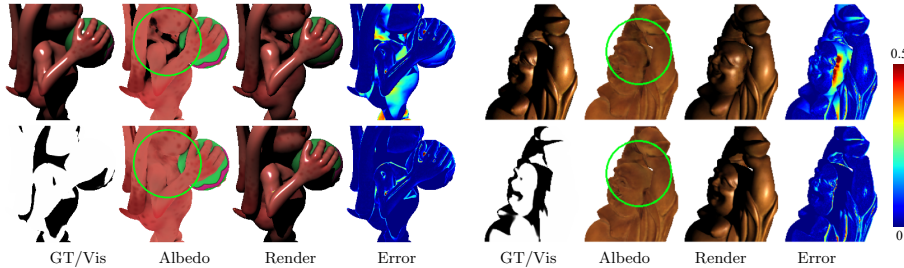


Fig. 7. Effectiveness of visibility modeling. (left: BUNNY, right: BUDDHA)

Evaluation on Synthetic Data Since existing neural rendering methods mainly assume a fixed environment lighting, we additionally evaluate on the synthetic dataset that is rendered with both PS lights (Synth^{PS} dataset) and environment light (Synth^{Env} dataset) to investigate the shape reconstruction performance under different light conditions.

The results in Table 4 reports similar geometry reconstruction performance for all baselines methods in both PS and environment lighting. They failed to reconstruct accurate surface in both light conditions. This may be due to the sparse input views, and the ambiguity in shape and material joint estimation, especially for non-textured regions, which exists in both PS and Env lightings. In contrast, our method successfully estimates more faithful geometry. We also show the qualitative comparison in Fig. 5. Our method achieves the best performance on both re-rendered quality and reconstructed surface normal, especially for details such as eye regions.

4.5 Method Analysis

Effectiveness of Normal Regularization Our method exploits multi-light images to infer surface normals to regularize the surface geometry in radiance field. It eliminates the ambiguity in density estimation especially for concave-shaped objects. We show the reconstruction results of before and after adding the normal constraint for both our method (*i.e.*, UNISURF [40] as our backbone of Stage I) and NeRF [36] on all objects in DiLiGenT-MV benchmark and *BUNNY* in Synth^{PS} dataset. As shown in Table 5 and Fig. 6, the introduced normal

Table 9. Quantitative results of different methods when trained with different number of views.

Method	BUNNY						ARMADILLO					
	Normal MAE ↓			Chamfer Dist ↓			Normal MAE ↓			Chamfer Dist ↓		
	5	15	30	5	15	30	5	15	30	5	15	30
PhySG [61]	34.53	25.69	27.25	36.75	21.87	42.25	30.81	19.53	20.19	49.38	12.08	16.60
UNISURF [40]	20.31	11.46	9.11	18.09	8.74	6.85	14.43	10.11	8.63	11.80	3.96	3.65
Ours	6.96	5.17	5.71	7.71	5.32	4.07	6.51	5.15	5.02	5.96	3.61	3.31

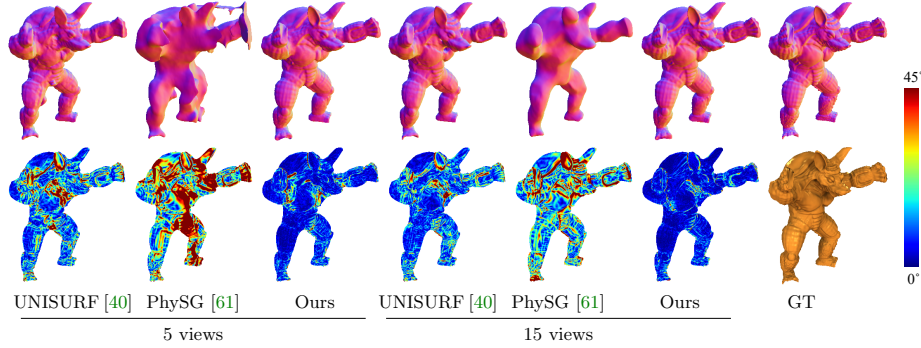


Fig. 8. Qualitative comparison on training with different number of views.

Table 10. Quantitative results of our method with different number of light directions.

N.light	Render			Normal MAE↓			Shape	Light Dir MAE↓	
	PSNR↑	SSIM↑	LPIPS↓	SDPS	Stage I	Ours	Chamfer Dist↓	SDPS	Ours
1	20.21	0.9686	2.08	48.52	17.81	14.21	11.94	47.22	3.82
2	20.69	0.9713	1.80	34.96	16.53	13.40	12.86	18.74	2.55
4	24.78	0.9855	0.84	14.76	9.20	6.75	7.37	10.32	1.59
8	25.84	0.9873	0.70	11.05	8.29	5.39	5.27	10.24	1.59
16	26.00	0.9876	0.69	10.86	8.07	5.30	5.43	9.71	1.31
32	26.03	0.9880	0.67	10.69	7.84	5.21	4.92	9.33	2.08
96	25.90	0.9873	0.68	10.65	7.74	5.18	5.32	8.96	1.53

regularization greatly improves the shape accuracy and recovered surface details for all objects. For example, on the *READING* object, NeRF decreases the normal MAE from 55.55 to 14.01 and UNISURF from 19.68 to 9.58, which verifies the effectiveness of the normal regularization.

Effectiveness of the Joint Optimization Benefiting from the rich shading information in multi-light images and our shadow-aware renderer, we are able to reconstruct faithful surface through joint optimizing normal, BRDFs and lights. Table 6 shows that joint optimization consistently improves the surface normal accuracy. Besides, the light directions are also refined through joint optimization as Table 7 shows.

We also investigated the design of our stage II by ablating the light direction optimization and visibility modeling. For ablation study on our own method, we calculate metrics of re-rendered images quality for each light sources instead of light-averaged image. Table 8 indicates that either fixing the initialized light direction or removing the visibility modeling will decrease the rendering quality and shape reconstruction accuracy. In particular, when light visibility is not being considered, the estimated albedo will be entangled with the cast-shadow, leading to inaccurate material estimation (see Fig. 7).

Effect of Training View Numbers Since our method can make full use of multi-light image to resolve the depth ambiguity in plain RGB image, it is able to reconstruct high-quality shape just from sparse views. To justify it, we compared our method with UNISURF [40] and PhySG [61] for surface reconstruction using 5, 15, and 30 training views. Note that the baseline methods were trained on Synth^{Env} dataset as they assume a fixed environment lighting. Table 9 and Fig. 8 show the reconstruction results using different number of views. Our method achieves satisfying reconstruction results even when only 5 views are given, whereas other methods all fail when view numbers are insufficient.

Effect of Light Direction Numbers While most previous PS methods requires calibrated lights, our method assumes uncalibrated lights and can handle an arbitrary number of lights. We also conduct experiments to explore how many light numbers are needed for reconstructing high-quality shapes, where 15 views are used. Similar to ablation study, we estimate per-light error for the re-rendered images. For light direction error, we take the mean values of their own used lights. Table 10 shows that increasing the number of lights generally increases the reconstruction accuracy. Our full method consistently outperforms SDPS-Net and Stage I under different number of lights. Given only 4 images illuminated under directional light for each view, our method achieves results comparable to that uses 96 images (*e.g.*, 6.75 vs. 5.18 for MAE), demonstrating the our method is quite robust to numbers of light directions.

5 Conclusions

In this paper, we have introduced a neural inverse rendering method for multi-view photometric stereo under uncalibrated lights. We first represent an object with neural radiance field whose surface geometry is regularized by the normals estimated from multi-light images. We then jointly optimize the surface normals, BRDFs, visibility, and lights to minimize the image reconstruction loss based on a shadow-aware rendering layer. Experiments on both synthetic and real dataset show that our method outperforms existing MVPS methods and neural rendering methods. Notably, our method is able to recover high-quality surface using as few as 5 input views.

Limitation Although our method has been successfully applied to recover high-quality shape reconstruction for complex real-world objects, it still has the following limitations. First, we ignore surface inter-reflections in the rendering equation. Second, we assume a solid object to locate its surface locations, thus cannot handle non-solid objects (*e.g.*, fog). Last, similar to most of the neural rendering methods, we assume the camera poses are given. In the future, we are interested in extending our method to solve the above limitations.

Acknowledgements This work was partially supported by the National Key R&D Program of China (No. 2018YFB1800800), the Basic Research Project No. HZQB-KCZY-2021067 of Hetao Shenzhen-HK S&T Cooperation Zone, NSFC-62202409, and Hong Kong RGC GRF grant (project# 17203119).

References

1. Agarwal, S., Furukawa, Y., Snavely, N., Simon, I., Curless, B., Seitz, S.M., Szeliski, R.: Building Rome in a day. *Communications of the ACM* (2011) [1](#)
2. Barron, J.T., Mildenhall, B., Tancik, M., Hedman, P., Martin-Brualla, R., Srinivasan, P.P.: Mip-NeRF: A multiscale representation for anti-aliasing neural radiance fields. In: *Proceedings of the IEEE/CVF International Conference on Computer Vision (ICCV)* (2021) [3](#)
3. Bi, S., Xu, Z., Srinivasan, P., Mildenhall, B., Sunkavalli, K., Hašan, M., Hold-Geoffroy, Y., Kriegman, D., Ramamoorthi, R.: Neural reflectance fields for appearance acquisition. *arXiv preprint arXiv:2008.03824* (2020) [4](#)
4. Boss, M., Braun, R., Jampani, V., Barron, J.T., Liu, C., Lensch, H.: NeRD: Neural reflectance decomposition from image collections. In: *Proceedings of the IEEE/CVF International Conference on Computer Vision (ICCV)*. pp. 12684–12694 (2021) [3](#), [7](#)
5. Boss, M., Jampani, V., Braun, R., Liu, C., Barron, J., Lensch, H.: Neural-PIL: Neural pre-integrated lighting for reflectance decomposition. In: *Proceedings of the Advances in Neural Information Processing Systems (NeurIPS)*. vol. 34 (2021) [3](#), [4](#), [10](#), [11](#), [23](#)
6. Chen, G., Han, K., Shi, B., Matsushita, Y., Wong, K.Y.K.: Self-calibrating deep photometric stereo networks. In: *Proceedings of the IEEE/CVF Conference on Computer Vision and Pattern Recognition (CVPR)*. pp. 8739–8747 (2019) [3](#), [5](#), [7](#), [8](#), [20](#), [24](#), [27](#)
7. Chen, G., Han, K., Shi, B., Matsushita, Y., Wong, K.Y.K.: Deep photometric stereo for non-Lambertian surfaces. *IEEE Transactions on Pattern Analysis and Machine Intelligence (T-PAMI)* **44**(1), 129–142 (2020) [3](#)
8. Chen, G., Han, K., Wong, K.Y.K.: PS-FCN: A flexible learning framework for photometric stereo. In: *Proceedings of the European Conference on Computer Vision (ECCV)*. pp. 3–18 (2018) [3](#)
9. Cheng, Z., Li, H., Asano, Y., Zheng, Y., Sato, I.: Multi-view 3d reconstruction of a texture-less smooth surface of unknown generic reflectance. In: *Proceedings of the IEEE/CVF Conference on Computer Vision and Pattern Recognition (CVPR)*. pp. 16226–16235 (2021) [3](#)
10. Chung, H.S., Jia, J.: Efficient photometric stereo on glossy surfaces with wide specular lobes. In: *Proceedings of the IEEE/CVF Conference on Computer Vision and Pattern Recognition (CVPR)* (2008) [3](#)
11. Esteban, C.H., Vogiatzis, G., Cipolla, R.: Multiview photometric stereo. *IEEE Transactions on Pattern Analysis and Machine Intelligence (T-PAMI)* (2008) [1](#), [3](#)
12. Furukawa, Y., Ponce, J.: Accurate, dense, and robust multiview stereopsis. *IEEE Transactions on Pattern Analysis and Machine Intelligence (T-PAMI)* **32**(8), 1362–1376 (2009) [1](#)
13. Garbin, S.J., Kowalski, M., Johnson, M., Shotton, J., Valentin, J.: FastNeRF: High-fidelity neural rendering at 200fps. In: *Proceedings of the IEEE/CVF International Conference on Computer Vision (ICCV)*. pp. 14346–14355 (2021) [3](#)
14. Hayakawa, H.: Photometric stereo under a light source with arbitrary motion. *JOSA A* (1994) [1](#)
15. Hertzmann, A., Seitz, S.M.: Example-based photometric stereo: Shape reconstruction with general, varying BRDFs. *IEEE Transactions on Pattern Analysis and Machine Intelligence (T-PAMI)* (2005) [3](#)

16. Hui, Z., Sankaranarayanan, A.C.: Shape and spatially-varying reflectance estimation from virtual exemplars. *IEEE Transactions on Pattern Analysis and Machine Intelligence (T-PAMI)* (2017) [3](#), [7](#), [25](#)
17. Ikehata, S.: CNN-PS: CNN-based photometric stereo for general non-convex surfaces. In: *Proceedings of the European Conference on Computer Vision (ECCV)* (2018) [3](#)
18. Ikehata, S., Aizawa, K.: Photometric stereo using constrained bivariate regression for general isotropic surfaces. In: *Proceedings of the IEEE/CVF Conference on Computer Vision and Pattern Recognition (CVPR)* (2014) [3](#)
19. Jakob, W.: Mitsuba renderer (2010) [9](#), [27](#)
20. Kajiya, J.T.: The rendering equation. In: *Proceedings of the 13th annual conference on Computer graphics and interactive techniques*. pp. 143–150 (1986) [6](#)
21. Kaya, B., Kumar, S., Oliveira, C., Ferrari, V., Van Gool, L.: Uncertainty-aware deep multi-view photometric stereo. *arXiv preprint arXiv:2010.07492* (2020) [3](#)
22. Kaya, B., Kumar, S., Oliveira, C., Ferrari, V., Van Gool, L.: Uncalibrated neural inverse rendering for photometric stereo of general surfaces. In: *Proceedings of the IEEE/CVF Conference on Computer Vision and Pattern Recognition*. pp. 3804–3814 (2021) [3](#)
23. Kaya, B., Kumar, S., Sarno, F., Ferrari, V., Van Gool, L.: Neural radiance fields approach to deep multi-view photometric stereo. In: *Proceedings of the IEEE/CVF Winter Conference on Applications of Computer Vision (WACV)*. pp. 1965–1977 (2022) [2](#), [4](#), [10](#), [11](#), [23](#)
24. Li, J., Li, H.: Neural reflectance for shape recovery with shadow handling. In: *Proceedings of the IEEE/CVF Conference on Computer Vision and Pattern Recognition (CVPR)* (2022) [7](#), [25](#)
25. Li, J., Robles-Kelly, A., You, S., Matsushita, Y.: Learning to minify photometric stereo. In: *Proceedings of the IEEE/CVF Conference on Computer Vision and Pattern Recognition (CVPR)* (2019) [3](#)
26. Li, M., Zhou, Z., Wu, Z., Shi, B., Diao, C., Tan, P.: Multi-view photometric stereo: a robust solution and benchmark dataset for spatially varying isotropic materials. *IEEE Transactions on Image Processing (TIP)* (2020) [1](#), [2](#), [3](#), [9](#), [22](#)
27. Li, Z., Sunkavalli, K., Chandraker, M.: Materials for masses: Svbrdf acquisition with a single mobile phone image. In: *Proceedings of the European Conference on Computer Vision (ECCV)*. pp. 72–87 (2018) [3](#)
28. Li, Z., Xu, Z., Ramamoorthi, R., Sunkavalli, K., Chandraker, M.: Learning to reconstruct shape and spatially-varying reflectance from a single image. *ACM Transactions on Graphics (TOG)* **37**(6), 1–11 (2018) [7](#)
29. Lim, J., Ho, J., Yang, M.H., Kriegman, D.: Passive photometric stereo from motion. In: *Proceedings of the IEEE/CVF International Conference on Computer Vision (ICCV)*. pp. 1635–1642 (2005) [3](#)
30. Liu, L., Gu, J., Lin, K.Z., Chua, T.S., Theobalt, C.: Neural sparse voxel fields. In: *Proceedings of the Advances in Neural Information Processing Systems (NeurIPS)*. vol. 33, pp. 15651–15663 (2020) [3](#)
31. Logothetis, F., Budvytis, I., Mecca, R., Cipolla, R.: Px-net: Simple and efficient pixel-wise training of photometric stereo networks. In: *Proceedings of the IEEE/CVF International Conference on Computer Vision*. pp. 12757–12766 (2021) [3](#)
32. Logothetis, F., Mecca, R., Cipolla, R.: A differential volumetric approach to multi-view photometric stereo. In: *Proceedings of the IEEE/CVF International Conference on Computer Vision (ICCV)*. pp. 1052–1061 (2019) [3](#)

33. Lu, F., Chen, X., Sato, I., Sato, Y.: SymPS: BRDF symmetry guided photometric stereo for shape and light source estimation. *IEEE Transactions on Pattern Analysis and Machine Intelligence (T-PAMI)* (2018) [3](#)
34. Martin-Brualla, R., Radwan, N., Sajjadi, M.S., Barron, J.T., Dosovitskiy, A., Duckworth, D.: NeRF in the wild: Neural radiance fields for unconstrained photo collections. In: *Proceedings of the IEEE/CVF Conference on Computer Vision and Pattern Recognition (CVPR)*. pp. 7210–7219 (2021) [3](#)
35. Mescheder, L., Oechsle, M., Niemeyer, M., Nowozin, S., Geiger, A.: Occupancy networks: Learning 3d reconstruction in function space. In: *Proceedings of the IEEE/CVF Conference on Computer Vision and Pattern Recognition (CVPR)*. pp. 4460–4470 (2019) [6](#), [8](#)
36. Mildenhall, B., Srinivasan, P.P., Tancik, M., Barron, J.T., Ramamoorthi, R., Ng, R.: NeRF: Representing scenes as neural radiance fields for view synthesis. In: *Proceedings of the European Conference on Computer Vision (ECCV)*. pp. 405–421 (2020) [2](#), [3](#), [4](#), [10](#), [11](#), [12](#), [20](#), [23](#)
37. Mukaigawa, Y., Ishii, Y., Shakunaga, T.: Analysis of photometric factors based on photometric linearization. *JOSA A* (2007) [3](#)
38. Nam, G., Lee, J.H., Gutierrez, D., Kim, M.H.: Practical svbrdf acquisition of 3d objects with unstructured flash photography. *ACM Transactions on Graphics (TOG)* **37**(6), 1–12 (2018) [3](#)
39. Niemeyer, M., Mescheder, L., Oechsle, M., Geiger, A.: Differentiable volumetric rendering: Learning implicit 3d representations without 3d supervision. In: *Proceedings of the IEEE/CVF Conference on Computer Vision and Pattern Recognition (CVPR)*. pp. 3504–3515 (2020) [2](#), [3](#), [6](#)
40. Oechsle, M., Peng, S., Geiger, A.: UNISURF: Unifying neural implicit surfaces and radiance fields for multi-view reconstruction. In: *Proceedings of the IEEE/CVF International Conference on Computer Vision (ICCV)*. pp. 5589–5599 (2021) [3](#), [5](#), [6](#), [8](#), [10](#), [11](#), [12](#), [13](#), [14](#), [20](#), [23](#), [25](#)
41. Park, J., Sinha, S.N., Matsushita, Y., Tai, Y.W., Kweon, I.S.: Robust multiview photometric stereo using planar mesh parameterization. *IEEE Transactions on Pattern Analysis and Machine Intelligence (T-PAMI)* (2016) [1](#), [2](#), [3](#), [9](#), [21](#), [22](#)
42. Reiser, C., Peng, S., Liao, Y., Geiger, A.: KiloNeRF: Speeding up neural radiance fields with thousands of tiny mlps. In: *Proceedings of the IEEE/CVF International Conference on Computer Vision (ICCV)*. pp. 14335–14345 (2021) [3](#)
43. Rusinkiewicz, S.M.: A new change of variables for efficient brdf representation. In: *Eurographics Workshop on Rendering Techniques*. pp. 11–22. Springer (1998) [7](#)
44. Santo, H., Samejima, M., Sugano, Y., Shi, B., Matsushita, Y.: Deep photometric stereo network. In: *Proceedings of the IEEE International Conference on Computer Vision Workshops (ICCVW)* (2017) [3](#)
45. Seitz, S.M., Curless, B., Diebel, J., Scharstein, D., Szeliski, R.: A comparison and evaluation of multi-view stereo reconstruction algorithms. In: *Proceedings of the IEEE/CVF Conference on Computer Vision and Pattern Recognition (CVPR)* (2006) [1](#)
46. Shi, B., Mo, Z., Wu, Z., Duan, D., Yeung, S.K., Tan, P.: A benchmark dataset and evaluation for non-Lambertian and uncalibrated photometric stereo. *IEEE Transactions on Pattern Analysis and Machine Intelligence (T-PAMI)* (2019) [1](#)
47. Sitzmann, V., Zollhöfer, M., Wetzstein, G.: Scene representation networks: Continuous 3d-structure-aware neural scene representations. *Proceedings of the Advances in Neural Information Processing Systems (NeurIPS)* **32** (2019) [3](#)

48. Srinivasan, P.P., Deng, B., Zhang, X., Tancik, M., Mildenhall, B., Barron, J.T.: NeRV: Neural reflectance and visibility fields for relighting and view synthesis. In: Proceedings of the IEEE/CVF Conference on Computer Vision and Pattern Recognition (CVPR). pp. 7495–7504 (2021) [3](#), [4](#), [7](#)
49. Taniyai, T., Maehara, T.: Neural inverse rendering for general reflectance photometric stereo. In: Proceedings of the ACM International Conference on Machine Learning (ICML) (2018) [3](#)
50. Tewari, A., Thies, J., Mildenhall, B., Srinivasan, P., Tretschk, E., Wang, Y., Lassner, C., Sitzmann, V., Martin-Brualla, R., Lombardi, S., et al.: Advances in neural rendering. arXiv preprint arXiv:2111.05849 (2021) [3](#)
51. Tozza, S., Mecca, R., Duocastella, M., Del Bue, A.: Direct differential photometric stereo shape recovery of diffuse and specular surfaces. *Journal of Mathematical Imaging and Vision* (2016) [3](#)
52. Wang, P., Liu, L., Liu, Y., Theobalt, C., Komura, T., Wang, W.: NeuS: Learning neural implicit surfaces by volume rendering for multi-view reconstruction. In: Proceedings of the Advances in Neural Information Processing Systems (NeurIPS). vol. 34 (2021) [3](#)
53. Wang, X., Jian, Z., Ren, M.: Non-Lambertian photometric stereo network based on inverse reflectance model with collocated light. *IEEE Transactions on Image Processing (TIP)* **29**, 6032–6042 (2020) [3](#)
54. Wang, Z., Bovik, A.C., Sheikh, H.R., Simoncelli, E.P.: Image quality assessment: From error visibility to structural similarity. *IEEE Transactions on Image Processing (TIP)* (2004) [8](#)
55. Wood, D.N., Azuma, D.I., Aldinger, K., Curless, B., Duchamp, T., Salesin, D.H., Stuetzle, W.: Surface light fields for 3d photography. In: Proceedings of the ACM SIGGRAPH Conference and Exhibition on Computer Graphics and Interactive Techniques in Asia (SIGGRAPH Aisa). pp. 287–296 (2000) [3](#)
56. Woodham, R.J.: Photometric method for determining surface orientation from multiple images. *Optical Engineering* (1980) [1](#)
57. Wu, C., Liu, Y., Dai, Q., Wilburn, B.: Fusing multiview and photometric stereo for 3d reconstruction under uncalibrated illumination. *IEEE Transactions on Visualization and Computer Graphics (TVCG)* **17**(8), 1082–1095 (2010) [3](#)
58. Wu, L., Ganesh, A., Shi, B., Matsushita, Y., Wang, Y., Ma, Y.: Robust photometric stereo via low-rank matrix completion and recovery. In: Proceedings of the Asian Conference on Computer Vision (ACCV) (2010) [3](#)
59. Wu, T.P., Tang, C.K.: Photometric stereo via expectation maximization. *IEEE Transactions on Pattern Analysis and Machine Intelligence (T-PAMI)* (2010) [3](#)
60. Yariv, L., Kasten, Y., Moran, D., Galun, M., Atzmon, M., Basri, R., Lipman, Y.: Multiview neural surface reconstruction by disentangling geometry and appearance. In: Proceedings of the Advances in Neural Information Processing Systems (NeurIPS). vol. 33, pp. 2492–2502 (2020) [2](#), [3](#)
61. Zhang, K., Luan, F., Wang, Q., Bala, K., Snavely, N.: PhySG: Inverse rendering with spherical gaussians for physics-based material editing and relighting. In: Proceedings of the IEEE/CVF Conference on Computer Vision and Pattern Recognition (CVPR). pp. 5453–5462 (2021) [3](#), [4](#), [7](#), [10](#), [11](#), [13](#), [14](#), [23](#)
62. Zhang, K., Riegler, G., Snavely, N., Koltun, V.: NeRF++: Analyzing and improving neural radiance fields. arXiv preprint arXiv:2010.07492 (2020) [3](#)
63. Zhang, R., Isola, P., Efros, A.A., Shechtman, E., Wang, O.: The unreasonable effectiveness of deep features as a perceptual metric. In: Proceedings of the IEEE/CVF Conference on Computer Vision and Pattern Recognition (CVPR). pp. 586–595 (2018) [8](#)

64. Zhang, X., Srinivasan, P.P., Deng, B., Debevec, P., Freeman, W.T., Barron, J.T.: NeRFactor: Neural factorization of shape and reflectance under an unknown illumination. *ACM Transactions on Graphics (TOG)* **40**(6) (2021) [3](#), [4](#), [7](#)
65. Zheng, Q., Jia, Y., Shi, B., Jiang, X., Duan, L.Y., Kot, A.C.: SPLINE-Net: Sparse photometric stereo through lighting interpolation and normal estimation networks. In: *Proceedings of the IEEE/CVF International Conference on Computer Vision (ICCV)* (2019) [3](#)
66. Zhou, Z., Wu, Z., Tan, P.: Multi-view photometric stereo with spatially varying isotropic materials. In: *Proceedings of the IEEE/CVF Conference on Computer Vision and Pattern Recognition (CVPR)*. pp. 1482–1489 (2013) [3](#)

Appendix

A More Details for the Proposed Method

A.1 More Details for Uncalibrated Photometric Stereo

We adopted a recent uncalibrated photometric stereo (UPS) method, called SDPS-Net [6], to estimate coarse surface normals and light directions. SDPS-Net is trained with a synthetic dataset, and we used the publicly available code and model for inference³.

For each view, SDPS-Net takes the multi-light images and the object mask as input, and estimate a surface normal map, light directions and light intensities.

A.2 More Details for Stage I

Network Architecture The network architecture of our Stage I is the same as UNISURF [40].

Training Details We use Adam as optimizer and set learning rate as 0.0001. For loss weight, we empirically adopt $\{1, 0.05, 0.005\}$ for α_{1-3} . Different from UNISURF [40], we utilized the normals estimated by SDPS-Net [6] to regularize the normals derived from the density field. The normal regularization loss was added after 1K iterations to stabilize the training. We trained Stage I for 100K iterations, which took about 12 hours to converge.

A.3 More Details for Stage II

Network Architecture We use 4-layer MLPs with width 128 for normal and albedo estimation, and a 2-layer MLPs with width 64 for predicting weights of specular SG basis. An 8-layer MLP with width 256 is used for visibility estimation. We add skip connection for normal, albedo and visibility MLPs at 2-th, 2-th and 4-th layer. We choose ReLU as the activation function.

Figure 9 shows the detailed network architecture of the four MLPs used in Stage II. We applied positional encoding with 10 frequency components to embed both input point \mathbf{x} and light direction \mathbf{w}_i into a higher dimensional space. The positional encoding is similar to [36]:

$$\gamma(p) = (\sin(2^0\pi p), \cos(2^0\pi p), \dots, \sin(2^{L-1}\pi p), \cos(2^{L-1}\pi p)). \quad (15)$$

The input of the four MLPs are the encoded point location $\gamma(\mathbf{x})$ and encoded light direction $\gamma(\mathbf{w}_i)$.

Training Details We use Adam as optimizer for stage II and set learning rate as 0.0005. For loss weight, we empirically adopt $\{1, 1, 1, 0.05, 0.01\}$ for β_{1-5} . To stabilize the training process, we first trained the normal MLP and visibility MLP for 5000 iterations, fixing weights of other MLPs and light parameters. We then jointly trained the normal, visibility, albedo, and specular MLPs, as well as optimize light parameters. We trained Stage II for 150K iterations, which took about 10 hours to converge.

³ <https://github.com/guanyingc/SDPS-Net>

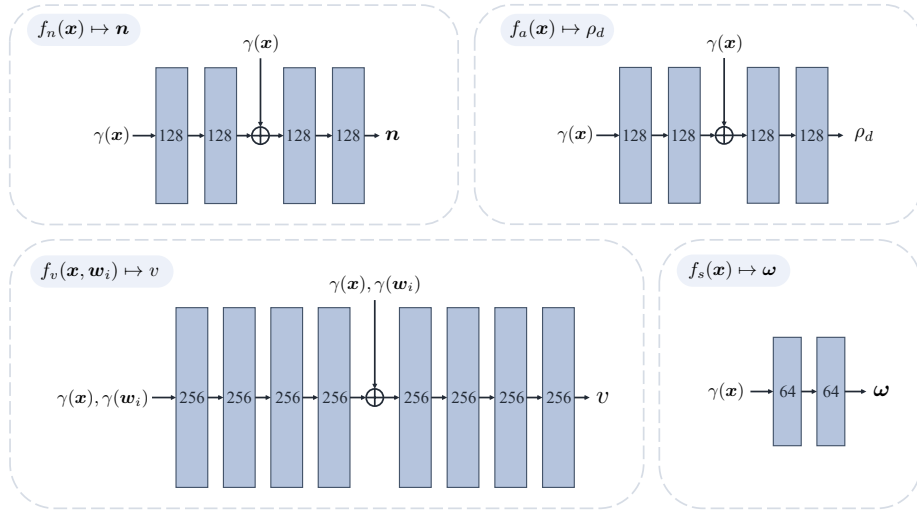


Fig. 9. Network architecture of the four MLPs in Stage II.

B More Details for the Comparison

B.1 Discussion for the Result on *COW*

Table 2 of the paper shows that our method performs slightly worse than PJ16 [41] on *COW* in the metric of Chamfer distances (i.e., 10.21 vs. 9.25). The main reason is that the camera poses in DiLiGenT-MV benchmark are located at the upper-hemisphere and slightly look downward, and the objects are placed on a desk with bottom part invisible. As a result, accurate reconstruction for the bottom part from images is impossible. Moreover, the bottom surface of *COW* is slightly concave, which further enlarges the final mesh error.

Figure 10 visualizes the mesh reconstruction error. We can see that our method achieves more accurate reconstruction on the visible surfaces, and most of the error are in the bottom regions.

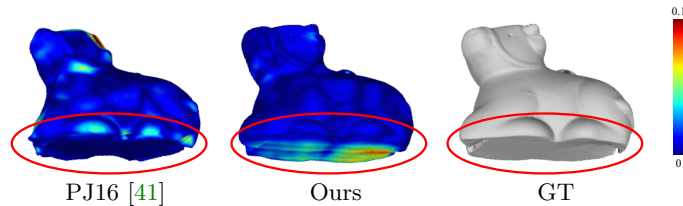


Fig. 10. Visualization of mesh reconstruction errors on *COW*. We can see that our method has larger errors on the bottom region, which is invisible in observed images and cannot be reconstructed accurately.

B.2 Discussion for the Mask Used in MAE Calculation

For fair comparison between different methods or analysis cases, we used the overlapped mask region for calculating the metrics. Therefore, there may be some small differences between the values shown in different tables.

In Table 2 of the paper, we measure the mean angular error (MAE) of the normal estimation using the intersection of input mask and our predicted mask. This is because our method reconstructs the full shape in a radiance field and uses projection to get image normals, the boundary regions might not be well aligned with the ground-truth mask. Figure 11 visualizes that when measures the normal estimation error with the ground-truth mask, our results will have a large error on the boundary region which has a thickness of about 1 pixel.

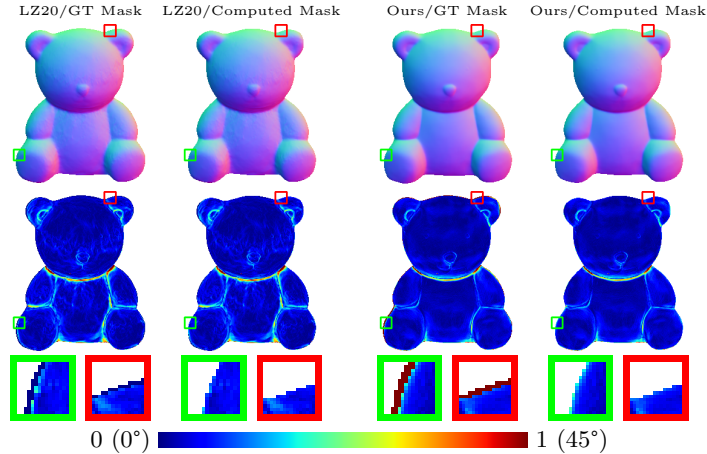


Fig. 11. Normal estimation error measured on the ground-truth mask and the computed mask of our method. As the computed mask is generate from the density field, there is a slight misalignment in the boundary region which increases the normal estimation error of our method.

We also show the normal MAE results measured on the ground-truth mask in Table 11. Despite having larger errors on the boundary, our method still achieves the lowest average MAE on DiLiGenT-MV benchmark, which clearly verifies the effectiveness of our method.

Table 11. Results of normal MAE calculated with GT mask.

Method	<i>BEAR</i>	<i>BUDDHA</i>	<i>COW</i>	<i>POT2</i>	<i>READING</i>	<i>Average</i>
PJ16 [41]	12.63	14.58	13.24	15.31	12.23	13.60
LZ20 [26]	4.45	11.64	4.13	6.79	8.74	7.15
Ours	4.39	11.31	4.79	6.29	8.89	7.13

B.3 More Comparisons with Neural Rendering Methods

More Qualitative Comparisons Figure 12 and Figure 13 show the visual comparisons on two objects from DiLiGenT-MV benchmark. Our method achieves the best rendering and normal reconstruction results.

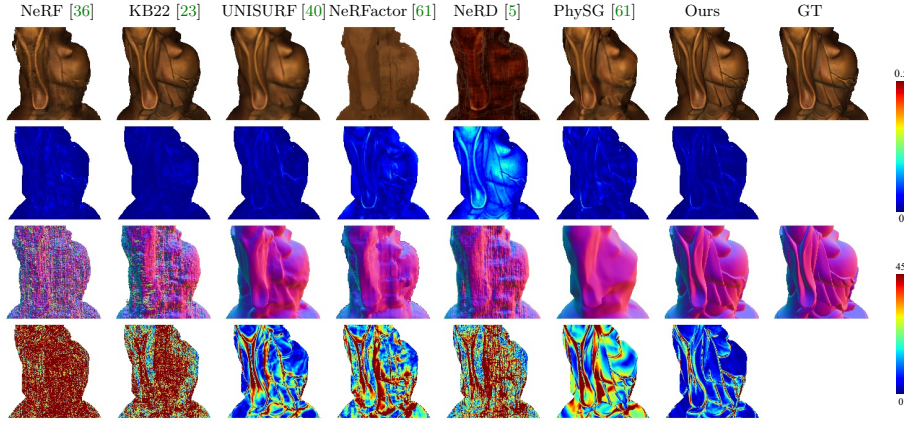


Fig. 12. More comparison with neural rendering methods on *BUDDHA* from DiLiGenT-MV benchmark.

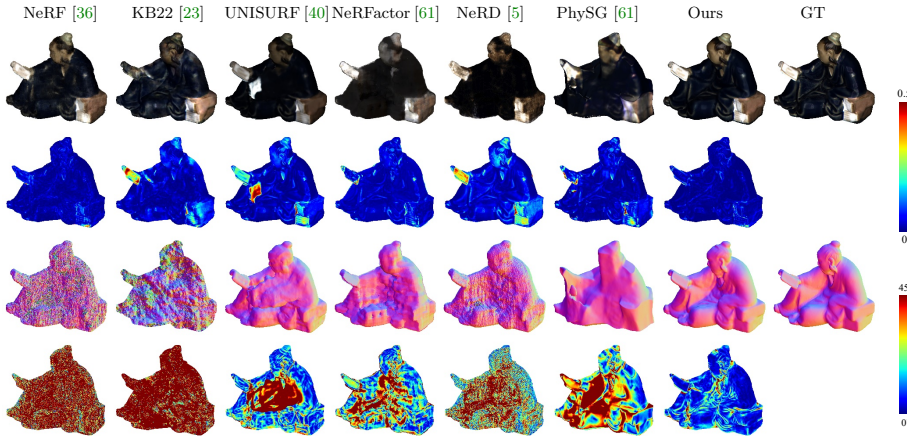


Fig. 13. More comparison with neural rendering methods on *READING* from DiLiGenT-MV benchmark.

C More Analysis for the Proposed Method

C.1 Improvement of Light Estimation

In Stage II, our method jointly optimizes the lights, normals and BRDFs. Table 12 shows the refinement of light direction and light intensity over the initialization estimated by SDPS-Net [6]. Our method significantly improves the estimation of SDPS-Net, reducing the the average MAE of light direction from 6.89 to 2.95, and average relative error of light intensity from 0.08 to 0.04.

Table 12. Improvement of light direction and intensity estimation compared to SDPS-Net [6].

Method	Light Direction MAE↓						Light Intensity Error↓					
	BEAR	BUDDHA	COW	POT2	READING	Average	BEAR	BUDDHA	COW	POT2	READING	Average
SDPS-Net	4.90	7.17	8.55	4.73	9.09	6.89	0.10	0.06	0.11	0.05	0.10	0.08
Ours	2.27	2.75	2.59	2.89	4.26	2.95	0.04	0.03	0.06	0.05	0.03	0.04

C.2 Effect of Different Combinations of View and Light Number

To further analyze the effect of input view and light numbers (*i.e.*, 5, 10, and 15). The camera distribution of the DiLiGenT-MV benchmark and the synthetic dataset are shown in Fig. 14.

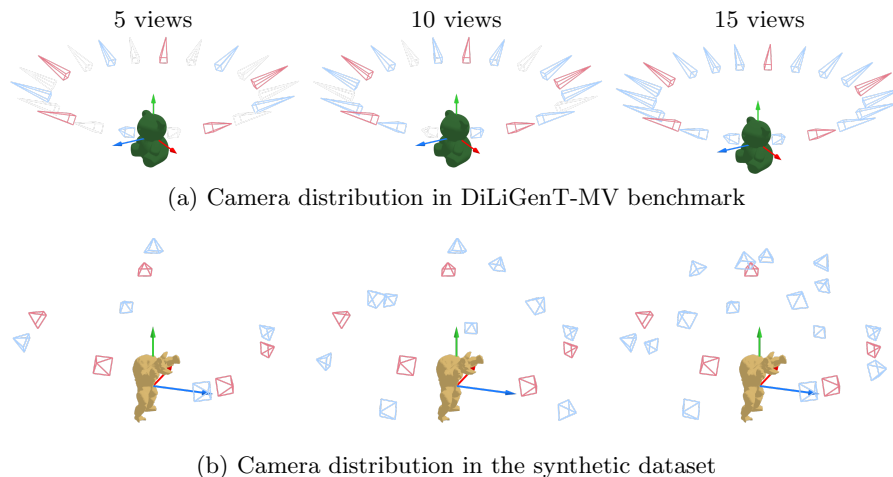


Fig. 14. Visualization of the camera distributions for setups with different input views. Training and testing views are shown in blue and red color, respectively.

For each input view number, we experimented with four different light numbers (*i.e.*, 2, 4, 8, and 16). Note that the test camera views are the same for all experiments.

Table 13 shows the normal estimation results of our method on two challenging objects (one real object *READING* and one synthetic object *BUNNY*) with different number of views and lights. We can see that given more input views and/or light numbers can improve the shape reconstruction results, and our method can achieve robust performance using just a sparse number of views and lights.

Take results on *READING* as an example, give 5 views and 8 lights, our method achieves a MAE of 11.52, which significantly outperforms existing neural rendering methods trained with 15 views (see Table 4 of the paper, where the best performing method UNISURF [40] achieves a MAE of 19.72).

Table 13. Results of our method on normal estimation error with different combinations of view and light numbers.

# Lights	READING			BUNNY		
	5 Views	10 Views	15 Views	5 Views	10 Views	15 Views
2	24.48	18.33	18.52	19.20	14.52	13.39
4	14.75	11.58	11.58	9.66	7.98	6.74
8	11.52	9.63	9.99	7.37	6.05	5.38
16	11.09	9.17	9.44	7.05	5.20	5.28

C.3 Effect of Different BRDF Parameterizations

As we found it difficult to model the specular effects of real-world objects by directly estimating the roughness parameter of the Microfacet model, we model the specular reflectance with a weighted combination of specular basis following [16,24]. Table 14 compares the results of methods using Microfacet model and specular basis on DiLiGenT-MV benchmark. We can see that the method using specular basis achieves better results in both image quality and shape reconstruction, which justifies the design of our method.

Table 14. Results of our method on DiLiGenT-MV benchmark with BRDF parameterizations.

BRDF Modeling	BEAR			BUDDHA			COW			POT2			READING			BUNNY			Average		
	PSNR \uparrow	SSIM \uparrow	MAE \downarrow	PSNR \uparrow	SSIM \uparrow	MAE \downarrow	PSNR \uparrow	SSIM \uparrow	MAE \downarrow	PSNR \uparrow	SSIM \uparrow	MAE \downarrow	PSNR \uparrow	SSIM \uparrow	MAE \downarrow	PSNR \uparrow	SSIM \uparrow	MAE \downarrow	PSNR \uparrow	SSIM \uparrow	MAE \downarrow
Microfacet	35.59	0.9836	3.21	28.96	0.9641	10.28	31.19	0.9754	4.21	39.45	0.9840	5.75	24.37	0.9692	9.07	22.76	0.9817	6.44	30.39	0.9763	6.49
Ours	35.67	0.9837	3.25	29.58	0.9670	10.20	37.06	0.9890	4.12	40.01	0.9860	5.73	24.89	0.9725	8.87	25.88	0.9871	5.24	32.18	0.9809	6.24

C.4 Effect of Different Material Types

To further investigate the results of our method on materials with different levels of specularity, we evaluated our method on *BUNNY* rendered with four strengths of specularity, ranging from diffuse to highly specular (denoted as A, B, C, and D). Table 15 and Fig. 15 show the results of our method on these four materials. We can see that our method achieves similar results on these four objects, indicating that our method is robust to different material types.

Table 15. Analysis on the effect of different material types on “*BUNNY*”.

Material Type	Render			Normal MAE↓			Shape		Light Dir MAE↓	
	PSNR↑	SSIM↑	LPIPS↓	SDPS	Stage I	Ours	Chamfer	Dist.↓	SDPS	Ours
A	27.79	0.9896	0.54	10.80	8.03	5.41	4.89		9.33	1.78
B	27.61	0.9896	0.53	10.31	7.58	5.38	4.77		9.30	2.57
C	26.97	0.9888	0.55	10.53	7.91	5.55	5.03		9.33	2.49
D	26.02	0.9879	0.67	10.69	7.86	5.22	4.92		9.33	2.08

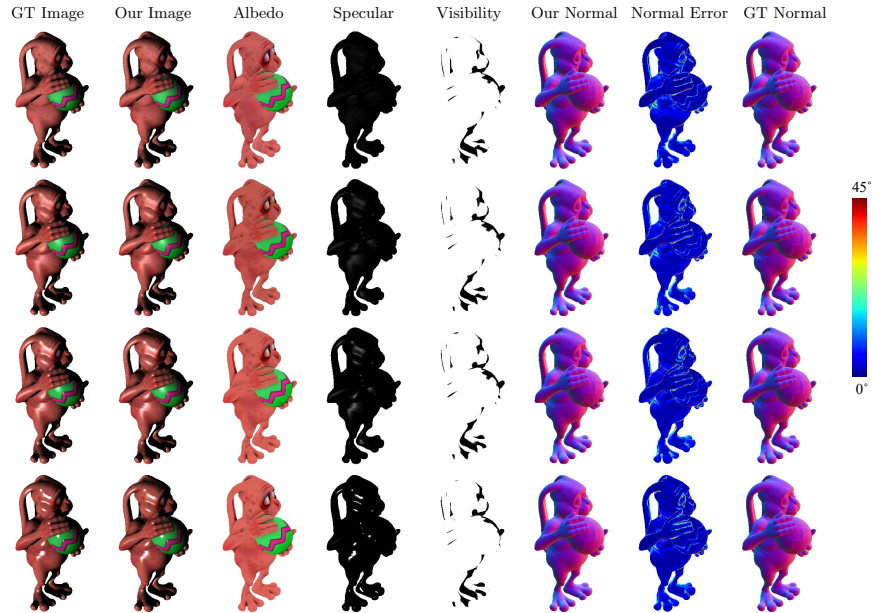


Fig. 15. Results of our method on materials with different levels of specularity. From top to bottom show the results on object A, B, C, and D. Column 1 shows the ground-truth image, and Column 2–6 show the rendered images, estimated albedo, specular component, visibility, and normals. Column 7–8 shows the normal estimation error and the ground-truth normals.

D More Details for the Datasets

D.1 Details of the DiLiGenT-MV Benchmark

Dataset Details DiLiGenT-MV benchmark contains five objects, called *BEAR*, *BUDDHA*, *COW*, *POT2*, and *READING*. For each object, images are captured from 20 evenly distributed cameras from the same elevation (see Fig. 16 (a)). For each view, 96 images are taken under different single directional lights with different light intensities (see Fig. 16 (b)).

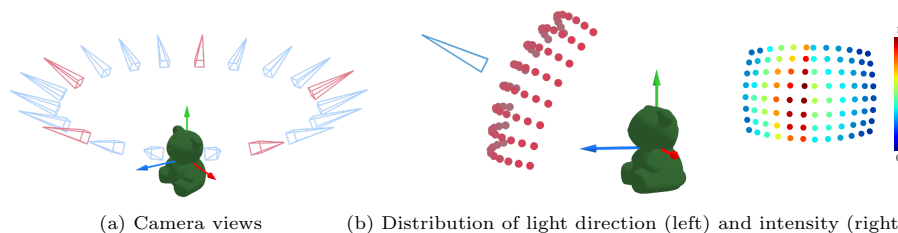


Fig. 16. Camera and light distribution in DiLiGenT-MV benchmark. The object is scaled up for $5\times$ for easier visualization. (a) The object is located at the origin, and the cones indicate the camera poses (blue for training and red for testing views). (b) For each view, 96 images under different single light directions are captured. At the left, the position of the red point indicates the light direction. At the right, the light intensities are normalized to $[0, 1]$ and visualized with pseudo color.

Data Processing Following conventional UPS setup, we assume an unknown white directional lights setup. As we do not have access to ground-truth light intensities, we normalize the original images with light intensities predicted by [6] when training Stage I. In Stage II, we will refine light intensities during the joint optimization. To train neural rendering methods on this dataset, we normalized images according to the ground-truth light intensities.

We cropped the original images with a resolution of 612×512 into 400×400 images to remove the background for each object.

D.2 Details of the Synthetic Dataset

Rendering Details We rendered two complex objects (*i.e.*, *BUNNY*⁴ and *ARMADILLO*⁵) under both PS lighting, denoted as Synth^{PS} dataset, and environment lighting, denoted as Synth^{Env} dataset, via Mitsuba [19]. The objects were rescaled to within a $[-1, 1]$ bounding box, and images with a resolution of 512×512 were rendered.

Camera & Light Distribution We used the same camera distribution for Synth^{Env} dataset and Synth^{PS} dataset. We randomly sampled 20 camera views

⁴ <https://www.cgtrader.com/free-3d-print-models/art/sculptures/all-your-egg-are-belong-to-us>

⁵ <http://graphics.stanford.edu/data/3Dscanrep/>

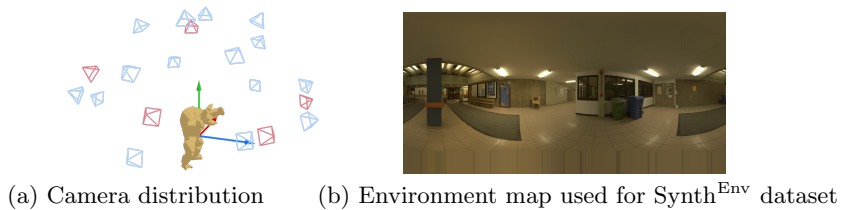


Fig. 17. (a) Camera distribution used in the synthetic dataset, where 15 training views are visualized in blue color and 5 testing view are in red color. (b) An environment map used for rendering Synth^{Env} dataset.

on the upper hemi- sphere, where 15 views for training and 5 views for testing (see Fig. 17 (a)). For Synth^{PS} dataset, we use the same light distribution as DiLiGenT-MV benchmark for each view, except that we set the same light intensity for each light. For Synth^{Env} dataset, we used an indoor environment map (see Fig. 17 (b)) for both objects.

E Applications

Our method jointly estimates surface normals, spatially-varying BRDFs, and lights. After optimization, the reconstructed object can be used for novel-view rendering, relighting, and material editing. Figure 18 shows the scene decomposition, material editing, and relighting results for a novel view of objects from DiLiGenT-MV benchmark.

Please check the supplementary video for more results.

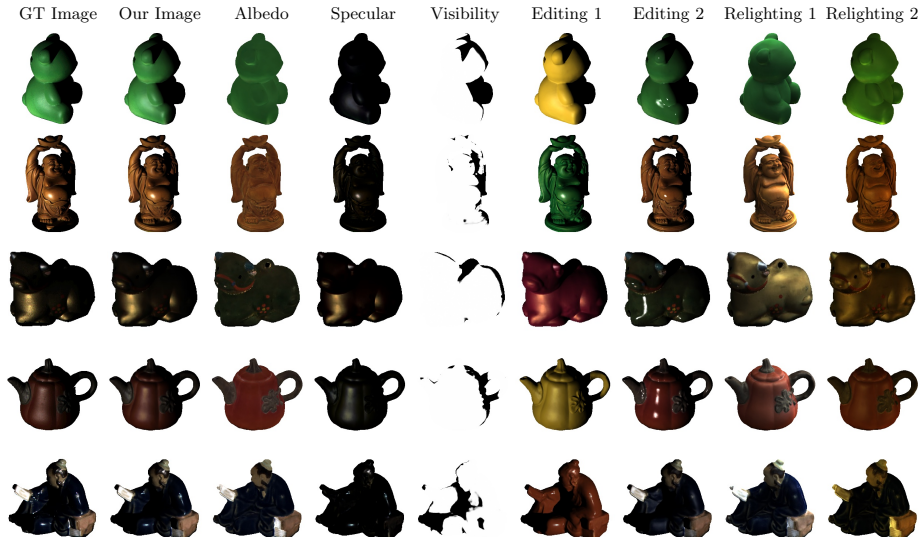


Fig. 18. Scene decomposition results of our method and applications. Columns 1–2 show the ground-truth and rendered images. Columns 3–5 show the reconstructed albedo, specular component, and visibility. Columns 6–7 edit the albedo and specular component of the objects, respectively. Columns 8–9 are two relighting results.